Article

Experimental Study on Grout–Soil Interaction Effects in Sandy Soil under Different Water-to-Cement Ratios

Huanxiao Hu [1,2], Yufan Lu [1,2], Chao Deng [3,*], Benqing Gan [1,2], Zhongliang Xie [1,2], Yuehui Cai [1,2] and Aikun Chu [1,2]

1   Key Laboratory of Metallogenic Prediction of Nonferrous Metals and Geological Environment Monitoring, Ministry of Education, Changsha 410083, China; hhx@csu.edu.cn (H.H.); 215011102@csu.edu.cn (Y.L.); 215012113@csu.edu.cn (B.G.); 215012123@csu.edu.cn (Z.X.); caiyuehui@csu.edu.cn (Y.C.); 225012142@csu.edu.cn (A.C.)
2   School of Geosciences and Info-Physics, Central South University, Changsha 410083, China
3   College of Civil Engineering, Hunan City University, Yiyang 413000, China
*   Correspondence: dengchao@hncu.edu.cn

Abstract: Due to the unique characteristics of sandy soil layers, there is often a coupling effect of multiple grout diffusion patterns in the grouting process, and different slurry diffusion modes may lead to different responses of soil structures. In this study, laboratory grouting model tests were conducted with homogeneous sand under different water-to-cement (w/c) ratios to reveal the temporal variations in grouting pressure, soil stress fields, and displacement fields during the grout diffusion process. The results show that, during the grouting process in the fine sand layer, the grout mainly exhibited a compaction–splitting diffusion mode. The farther away from the grouting center, the more pronounced the hysteresis effect of soil pressure caused by grout diffusion. Meanwhile, as the w/c ratio increased, the diffusion mode between the slurry and the soil was in a transitional state. At $w/c > 1.2$, the primary pattern changed from the fracture–compaction pattern to the permeation–fracture–compaction pattern and fracture–permeation pattern. And the overall trend of the grouting pressure curve was similar under all of the w/c ratio conditions, showing a trend of increasing to the maximum value of the pressure first and then decreasing. With the increase in the water–cement ratio, the overall value of the grouting pressure curve showed a decreasing trend, the pressure value increased more slowly with time before reaching the maximum value, and the more obvious the influence of water–cement ratio was when $w/c > 1.2$. Additionally, the surface displacement also exhibited an overall decreasing trend, and it had no obvious lifting value under the condition of $w/c = 1.6$.

Keywords: grouting in homogeneous sand; water-to-cement ratio; stress fields; displacement fields; temporal variations; grout–soil interaction effects

1. Introduction

Grouting is a cost-effective geotechnical engineering technique that has been extensively applied and developed in the field of foundation treatment in recent decades. It is one of the most commonly used methods in the reinforcement of sandy soil foundations, which and can effectively enhance the mechanical properties and waterproofing performance of sandy soil foundations [1–4].

Due to the porous nature of sandy soils, the injectability of the sand layer and the grouting pressure determine the diffusion and reinforcement modes of sand grouting [5–7]. As a result, various diffusion patterns, such as permeation, compaction, and fracture, may occur during the grouting process. Currently, most of the experimental studies on sand grouting concentrate on the diffusion pattern of permeation grouting, which initially involved the characterization of effects of grout properties (e.g., particle size and w/c ratio), sand layer properties (e.g., particle size distribution and permeability), and grouting

pressure on grout diffusion and reinforcement [8–12]. And then, the studies delved into the time-varying viscosity for different grout flow regimes, the filtration effect in porous sandy media, and the diffusion mechanism of the grout for grout diffusion paths [13–17]. The above studies mainly focused on the diffusion of grout in the pore space of sandy soil stratum, during which the grout had no obvious effect on the sand skeleton.

For the compaction and fracture diffusion patterns, the sand skeleton deforms under grouting pressure and slurry, which is commonly used for controlling ground settlement, raising structures, and soil compaction reinforcement [18–22]. Through laboratory simulation experiments, Zhang et al. experimentally revealed the effect of the *w/c* ratio on the grout diffusion patterns, and they demonstrated that the grout diffusion pattern changes from compaction-dominated to fracture-dominated with increasing *w/c* ratio [23]. On this basis, Wang et al. investigated the effects of *w/c* ratio and soil saturation on the grout diffusion pattern in sandy soil under pressure grouting conditions [24]. The experiments performed by Ye et al. further demonstrated that the initial soil saturation significantly affected the injectability of sandy soil, and thus the formation of grout bubbles [25]. Practical experiences indicate that the fracture–compaction grouting pattern plays an important role in sand grouting engineering [26]. For this grouting pattern, Li et al. conducted experiments using a three-dimensional simulation test system to study the grout diffusion patterns during repeated fracturing grouting in fault fracture zones and revealed the characteristics of the stress field response during the grouting process [27]. In addition, Zhang et al. established a theoretical model of fracture grout diffusion that considers the nonlinear compression characteristics of the sandy soil and conducted grouting experiments on the compaction characteristics of sandy soil to analyze the fracture–compaction grout diffusion process from the perspective of the sand skeleton [28–30]. Qin et al. studied the compaction properties of sandy soil by adjusting the clay content and initial water content, and analyzed the influence of clay content on fracturing grout diffusion [31]. The aforementioned research initially focused on the analysis of the diffusion process of injected slurry and gradually developed to consider the mutual interactions between soil and injected slurry. However, the grouting process is a dynamic process of soil–grout interaction, which often involves the combined action of multiple modes (especially in sandy soils). Available studies have not systematically explored this aspect, and there is a need for a further detailed exploration of the dynamic response of the grout–soil interaction process in sandy soil grouting.

In this paper, the dynamic interaction between slurry and soil during the diffusion of slurry with different water–cement ratios was investigated using homogeneous sandy soil as the experimental object. Considering that it is difficult to maintain stable pressure conditions during the actual grouting process, the grout flow rate was controlled in the experiments. A self-developed laboratory grouting model was used to conduct grouting tests under different *w/c* ratios on sandy soil layers. The study recorded and analyzed the stresses and strains in the sandy soil, and clarified the diffusion patterns of the slurry during the grouting process. Temporal variations of the soil stress and displacement fields under corresponding grouting pressure conditions were obtained, and the influence of different *w/c* ratios on the grout diffusion process as well as the corresponding stresses and strains in the sand layer was analyzed.

2. Experimental Apparatus and Test Methods

2.1. Grouting Test Apparatus

The test device consisted of a power and circulatory system, a soil-simulation system, and a monitoring and recording system, as presented in Figure 1. The test involved injecting the slurry into the sandy soil layer during the grouting process using a flow-controlled grouting pump with a consistent grout flow rate.

The grouting power system of the apparatus utilized a flow-controlled grouting pump with an operating pressure range of 0–10 MPa and an operating flow rate of 8.5 mL/s. The purpose of the cyclic test system was to evacuate air from the conduit before the test and to test the grouting pressure gauge for proper operation. The soil simulation system

was a visualized cylindrical model test bucket with an inner diameter of 350 mm and a height of 700 mm, which was connected to a grouting pipe with an inner diameter of 20 mm at the bottom. The data measurement and recording system consisted of measuring instruments (pore water pressure sensor, soil stress sensor, and displacement sensor) and data acquisition instruments (data dynamic recorder, CCD camera, and PC recording terminal). The measurement instruments and their locations are illustrated in Figure 2. The measurement instruments were attached by means of rigid steel rods with a diameter of 5 mm and a length of 460 mm, which could be fixed to the bottom of the bucket. The relevant test parameters and the corresponding numbers of each measurement instrument are shown in Table 1 below.
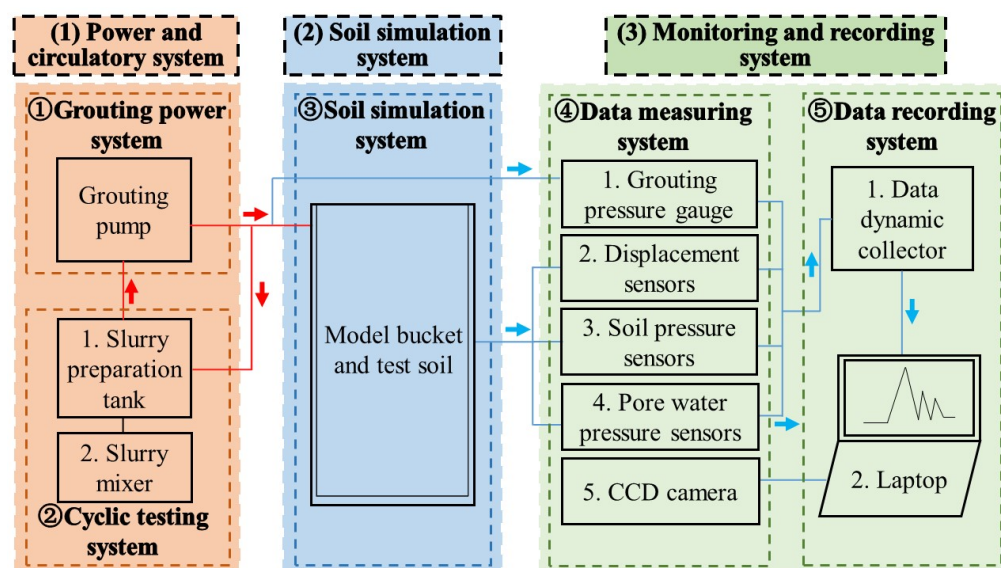

Figure 1. Schematic diagram of the experimental apparatus and flow process (red arrows represent the slurry flow path and blue arrows represent the data flow path).

The power circulatory system and soil simulation system were connected by pipelines, and the power circulatory system and soil simulation system were connected to the data measuring system by data lines. The final whole setup is depicted in Figure 3. Since the test soil was a sandy soil layer, the loose characteristics of the soil could not guarantee the normal grouting test process from top to bottom, so the slurry injection position was set at the bottom of the bucket. The grouting pipe with an inner diameter of 20 mm was connected to the bottom of the bucket, and the bottom-up slurry-injection method was adopted to carry out the grouting test.

Table 1. Parameters of each measuring instrument.

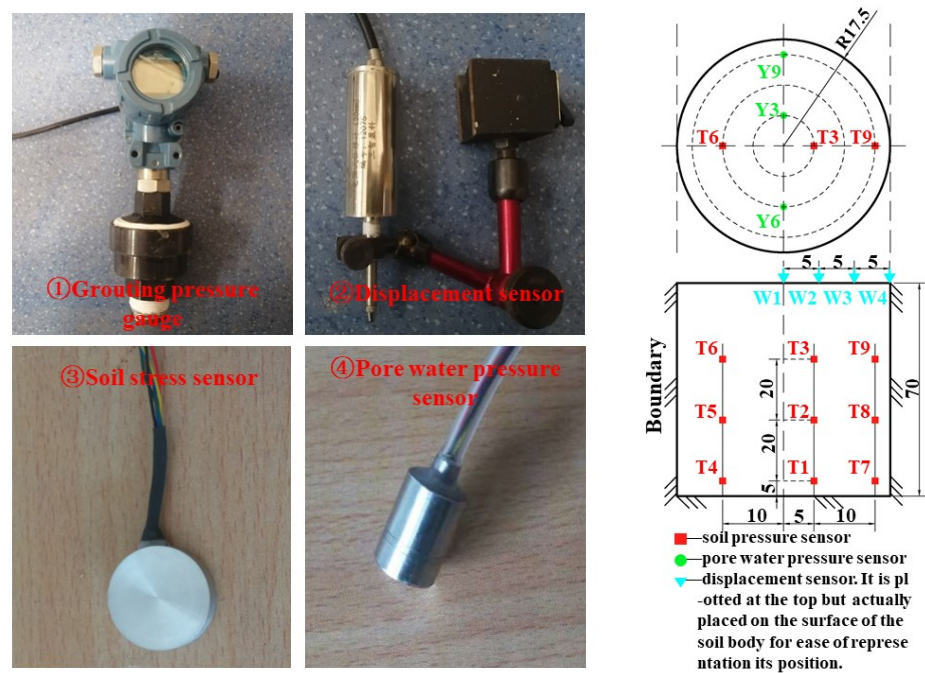| Name of Instrument	Corresponding Number in Figure 2	Range	Accuracy
① Grouting pressure gauge	-	02.5 MPa	0.5%FS
② Displacement sensor	W1-W4	0–20 mm	0.3%FS
③ Soil stress sensor	T1-T9	0–0.2 MPa	0.3%FS
④ Pore water pressure sensor	Y1-Y9	0–0.1 MPa	0.5%FS

Figure 2. Appearance and arrangement of measurement instruments (unit: cm.).

Figure 3. Flowchart and physical diagram of the experimental apparatus (the serial numbers in the figure correspond to those in Figure 1).

2.2. Experimental Materials and Methods

2.2.1. Grouting Material

Ordinary Portland cement P·O42.5 was adopted for the test. Its initial and final setting times were 185 min and 234 min, respectively; and its 3-day and 28-day compressive strengths were 27.6 MPa and 46.7 MPa, respectively.

2.2.2. Experimental Soil

Sandy soil layers were selected as the research subject. To control the properties of the soil to be grouted, standard sand was used for the test. The particle size distribution of the standard sand is displayed in Figure 4, with a uniformity coefficient (C_u) of 6.92 and a curvature coefficient (C_c) of 1.97, which indicated that it was fine sand with good grading. The specific gravity (G_s) of the sand was 2.635 g/cm^3, and its water content was mixed to 6%. To ensure the relative uniformity of the soil, a specific mass of sand was loaded into buckets in layers and compacted to 50 mm per layer to control its density to

1.65 g/cm³ and porosity to 0.693. The surface of each layer was roughened before adding the next layer, increasing the surface roughness and bonding between layers until the final height was 650 mm. Geotechnical tests indicated that the cohesive strength (*c*) of the prepared experimental sand was approximately 10 kPa and the internal friction angle (*φ*) was approximately 38°.
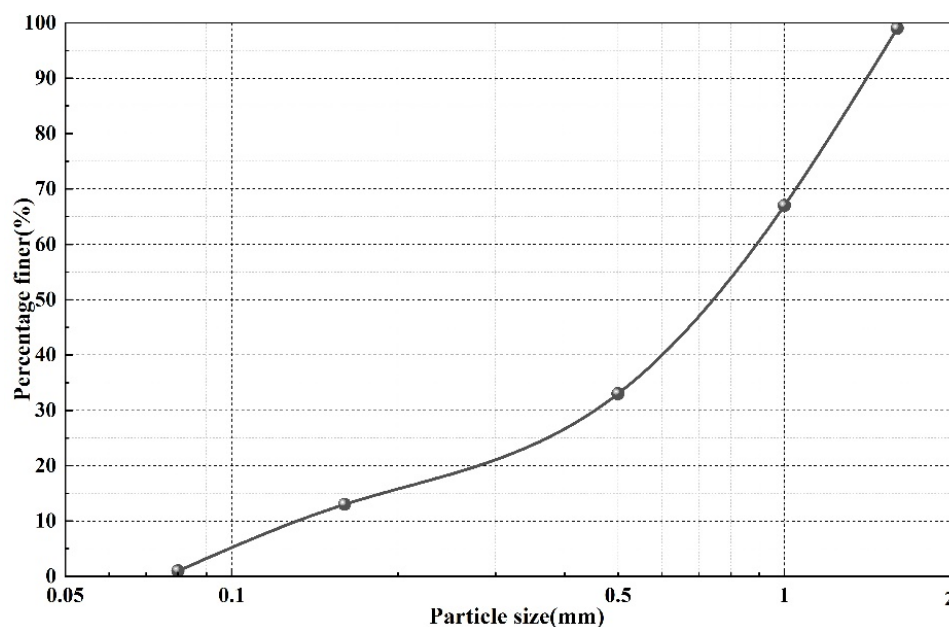

Figure 4. Cumulative particle size distribution curve of standard sand.

2.2.3. Regulation of Grouting

The tests were conducted using a flow-controlled method, and the measured grouting flow rate output from the grouting pump was 8.5 mL/s. Grouting was performed using grout with different *w/c* ratios, which were set at 0.8, 1.0, 1.2, 1.4, and 1.6. The basic physical properties of the grout with different *w/c* ratios are summarized in Table 2.

Table 2. Basic physical properties of grout with different *w/c* ratios.

w/c **Ratio**	**Density (g/cm³)**	**Stone Rate (%)**
0.8	1.55	83
1.0	1.47	76
1.2	1.39	61
1.4	1.36	59
1.6	1.33	51

3. Evolution of Stress and Displacement Fields in Sand Layer

3.1. Variations in Grouting Pressure and Surface Displacement with Grouting Time

The grouting pressure–time curve (*P-t*) and the surface uplift displacement versus time curve (*u-t*) (i.e., the *P-u-t* curve) plotted in Figure 5 for the low-*w/c*-ratio condition (*w/c* = 0.8) indicated that the grouting process can be divided into three phases.

3.1.1. Early Stage: Initial Uplift Phase Dominated by Compaction

In the early period of this phase within 0 to 40 s, the grout filled the grouting hole. At this time, the grouting diffusion resistance was not significant, resulting in little change in grouting pressure and no surface displacement.

In the middle period of this phase, from 40 to 80 s (duration of 40 s), under the influence of grouting pressure, grout began to interact with the surrounding sand particle skeleton. The diffusion resistance of the grout increased rapidly, leading to the compaction

of the soil around the grouting hole. The density of the soil increased and its internal skeleton deformed. At this point, the volume of grout injected into the soil was equal to the volume of the compressed soil. The effect of the internal skeleton deformation could not be transmitted to the upper surface of the soil, so the grouting pressure continued to increase rapidly without significant uplift displacement.
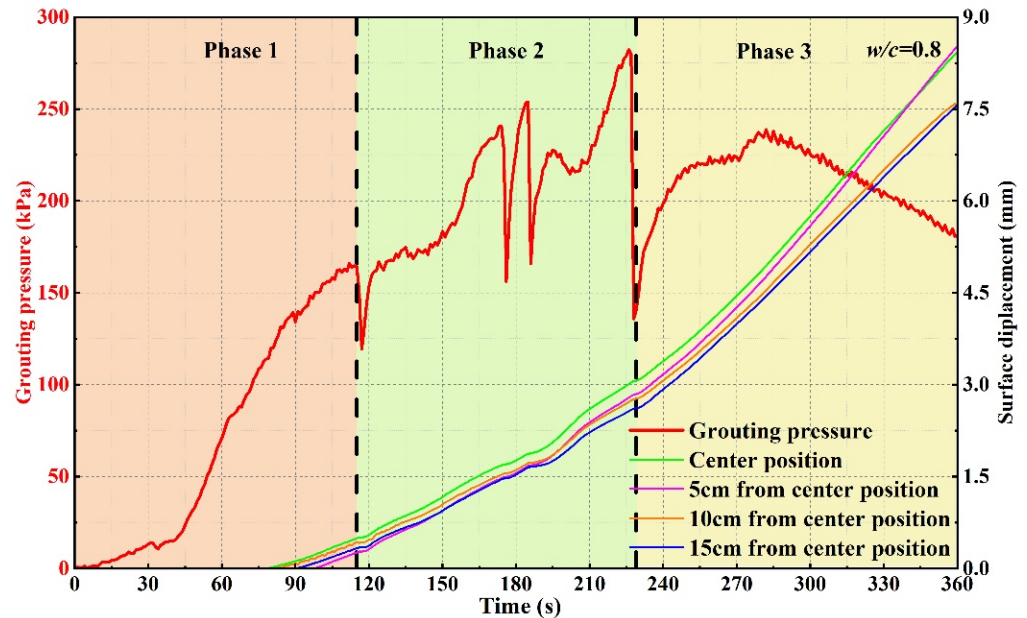

Figure 5. Time-dependent curves of grouting pressure and displacement at a *w/c* ratio of 0.8.

In the later period of this phase, from 80 to 115 s (duration of 35 s), grout continued to compress the soil under the action of the grouting pressure. At this point, the volume injected into the soil exceeded the volume of compressed soil. The surface soil was affected, leading to deformations and an increase in surface displacement. During this period, the grouting pressure continued to increase, and the uplift displacement at various surface locations also increased until the grouting pressure reached a local maximum.

3.1.2. Medium Term: Sustained Uplift Phase of Fracture–Compaction

In the early period of this phase, from 115 to 117 s (duration of 2 s), the grouting pressure decreased significantly after a local maximum and reached a local minimum. There was a short plateau period in the surface displacement. It is evident that compaction grouting was the primary diffusion pattern between the grout and the soil, as demonstrated by the composition of the grout-solidified body in Section 4.1. The probable reasons for the decrease in grouting pressure were as follows: (1) The presence of a weak structure within the soil during grouting led to the slurry entering the weak structure while diffusing, which resulted in a reduction in the force exerted on the soil, a decrease in grouting pressure, and a plateau period in surface displacement. (2) Following the previous phase of grouting, the slurry continued to exert pressure on the adjacent soil. The stress state of the soil gradually transformed from compression to tension until the grouting pressure reached the condition of soil fracture, resulting in soil fracture due to tensile damage. The fracture surface occurred at the principal stress surface of least resistance. When the soil fractured, the grout quickly filled the fracture channel, and stress concentration happened at the front end of the fracture, resulting in the rapid development of the fracture. As a result, the grouting pressure diminished until it reached a local minimum, and the surface displacement yielded a plateau period.

In the later period of this phase from 117 to 175 s (duration of 57 s), the grouting pressure rose again after the local minimum until the second local maximum and minimum occurred. The surface displacement increased with increasing grouting pressure until the

local extrema of grouting pressure, and then exhibited a plateau period during the extrema period of grouting pressure, which was the same as the first phase of the local extrema of grouting pressure. The extrema phase of the grouting pressure curve and the plateau period of the surface displacement curve showed an inhomogeneous cyclic variation pattern in the subsequent process from 175 to 230 s (duration of 55 s), with an increasing trend in the local maximum of the grouting pressure. Examination of the solidified body (see Section 4.1), grouting pressure, and ground displacement curve under the test condition of *w/c* = 1.0 (see Figure 6) revealed that compaction was the dominant pattern between the grout and the soil. Meanwhile, the change patterns of the grouting pressure curve and the surface displacement curve were similar to the non-uniform cyclic change pattern at *w/c* = 0.8, and the local maximum of the grouting pressure also showed an upward trend, which was judged to be the typical fracture–compaction pattern in the sand grouting process. The reason why the grouting pressure rose again after the local minimum and showed an increasing trend in the local maximum was as follows. As the fracture developed, the grout continued to act on the soil on both sides of the fracture, at which point it entered the expansion phase of the fracture channel. Since the soil had been compacted under pressure in the previous phase, its overall resistance to deformation increased, and thus a higher grouting pressure was required to widen the fracture channel or create new ones. Therefore, the grouting pressure rose after the local minimum happened and exceeded the previous local maximum until the subsequent soil-fracturing pressure condition was attained, with a corresponding trend of increasing displacement.
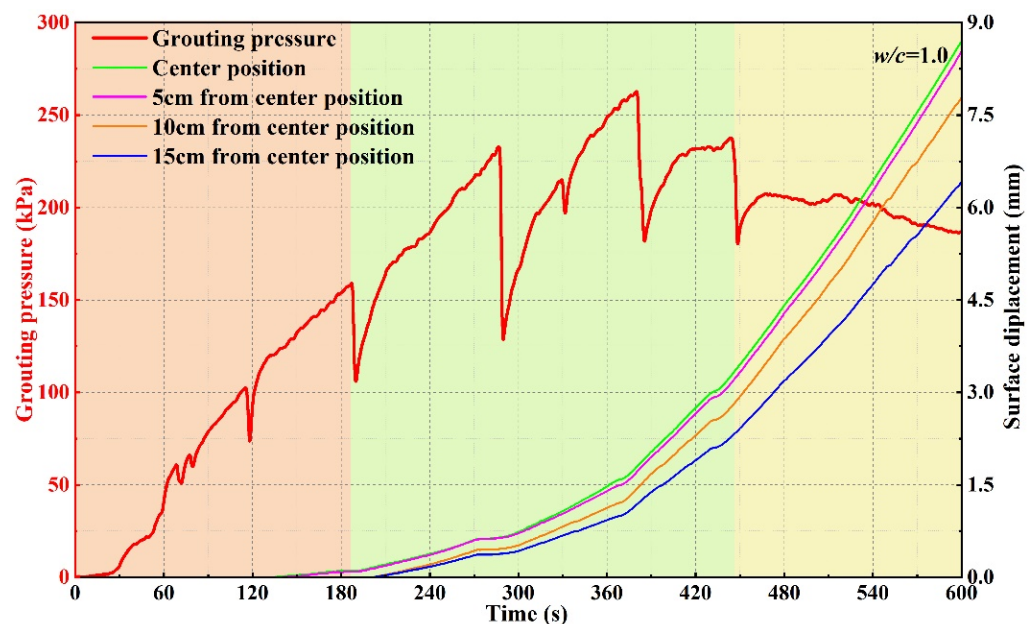

Figure 6. Time-dependent curves of grouting pressure and displacement at a *w/c* ratio of 1.0.

3.1.3. Late Stage: Accelerated Uplift Phase of Shear Damage

As the grouting process proceeded to a certain phase, the grouting pressure increased from a local minimum to a certain value and then began to decrease. The final shape and structure of the solidified body in Section 4.1 indicated that the grout continued to exert pressure on the surrounding soil under the grouting pressure. The soil reached its compression limit, and the overlying soil was unable to provide the stress conditions to reach the fracturing pressure. Consequently, continued grouting led to shear damage in the soil, resulting in a decrease in grouting pressure and a further increase in surface displacement.

As shown in the *P-u-t* curve in Figures 5 and 6: (1) The grouting pressure curve repeatedly reached local extrema and the corresponding surface displacement curve entered a plateau period, which suggested that grout diffusion channels were formed due to soil

fracture and was a key indicator reflecting the occurrence of the soil fracture process. (2) Both the grouting pressure curve and surface displacement curve in the fracture phases exhibited a pulse-like pattern and were in the cyclic state of uneven changes, i.e., the magnitude of the extremum of the grouting pressure, the time interval to reach the extremum, and the duration of the extrema period were both different in each cycle. (3) During the grouting process, the local maximum of the grouting pressure (fracture pressure) increased with increasing grouting time.

3.2. Variation of Soil Pressure with Time

Since a relatively low pore water pressure was measured during the experiments, its impact on the testing process was minimal. Therefore, an analysis of the soil pressure within the soil was conducted, and the arrangement of sensors is depicted in Figure 2.

3.2.1. Radial Location

As shown in Figure 7, by comparing the soil pressures at the locations with the same vertical heights (*H*) from the bottom of the bucket, it can be observed that the time at which the soil skeleton experienced compression-induced soil pressures became later as the radial distance (*D*) from the center of the grouting hole increased. This indicated that the influence range of the grout on the soil mass in the radial direction gradually expanded with increasing grouting time. Moreover, the overall soil pressures decreased with the increase in distance *D*. This implied that the action of the grout led to the deformation of the soil near the grouting holes, which, in turn, affected the soil around them and the forces acting on the soil were dispersed. Consequently, the soil pressures decreased with increasing distance from the grouting hole, and the soil was affected to an increasing range.
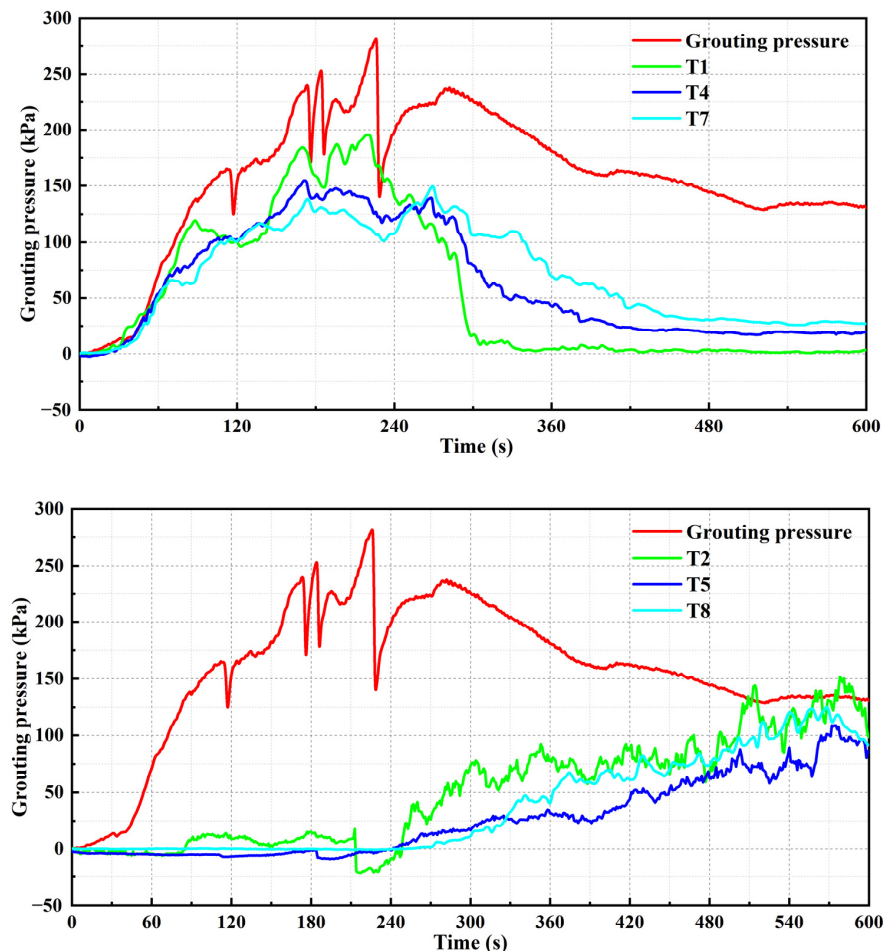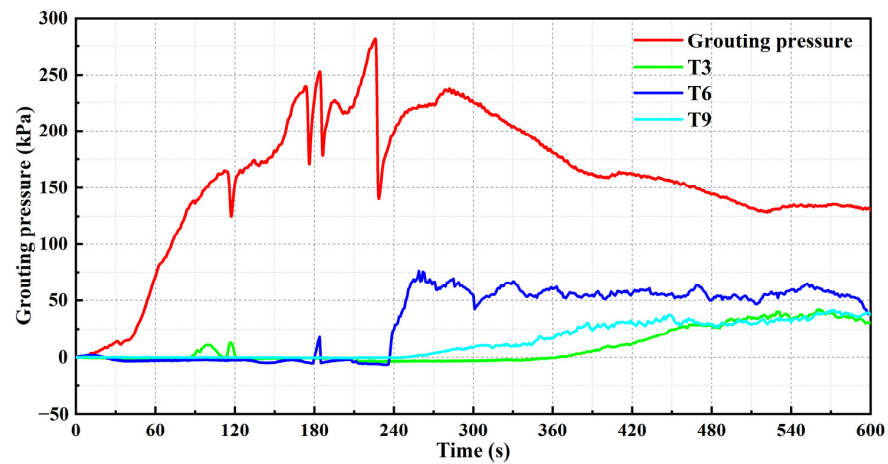

Figure 7. *Cont.*

Figure 7. Comparison of soil pressure at vertically identical height (*H*) from the bottom of the bucket.

3.2.2. Vertical Location

The soil pressures at the same radial distance (*D*) from the center of the grouting hole are shown in Figure 8. The change rule was similar to that of the vertical direction, i.e., the higher the *H* from the bottom of the bucket, the later the time point when the soil pressure was generated, and the smaller the overall soil pressure.
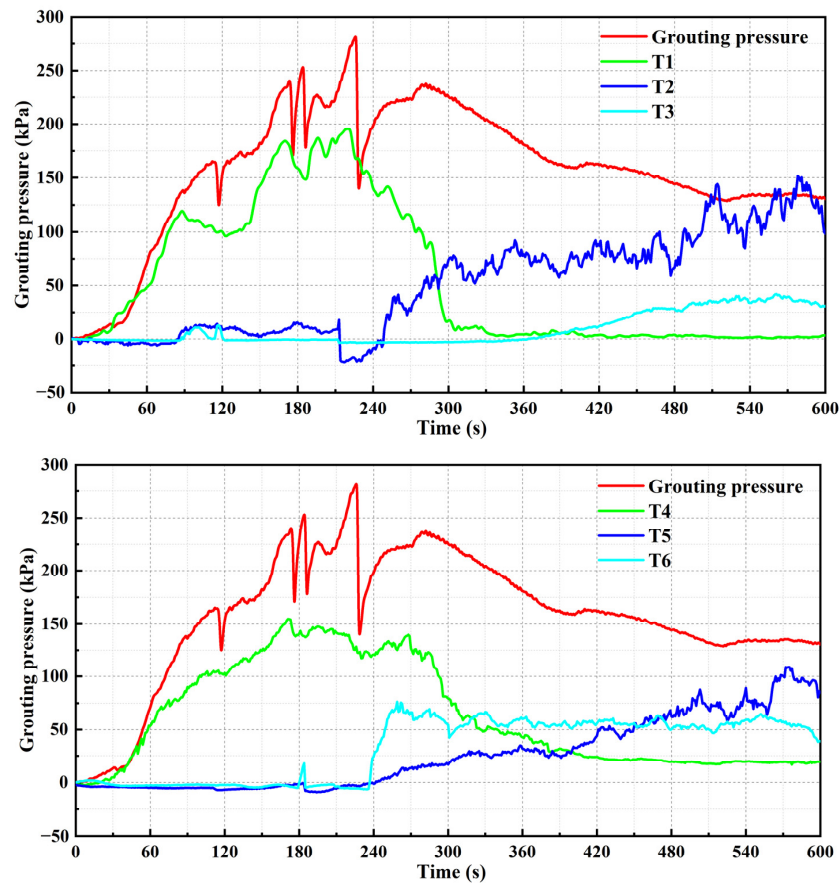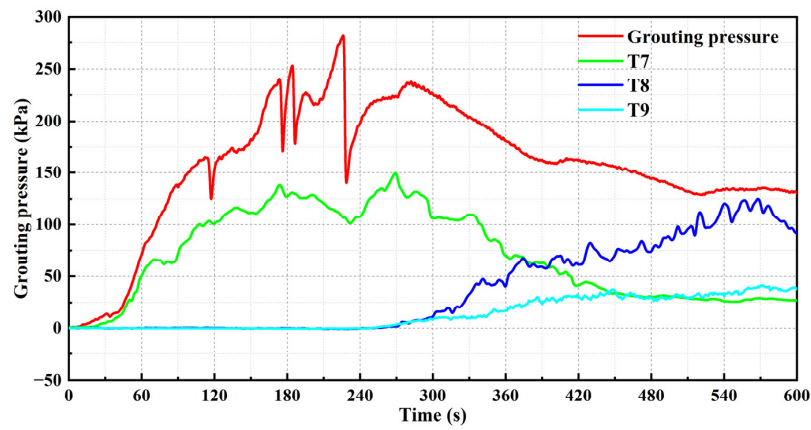

Figure 8. *Cont.*

Figure 8. Comparison of soil pressure at radially identical distance (*D*) from the grouting hole.

4. Influence of *w/c* Ratio on the Evolution of Stress and Displacement Fields in Sand

4.1. Differences in Grouting Patterns

The solidified bodies with different *w/c* ratios were compared in conjunction with the injectability of the sandy soil. The pattern differences between the slurry and the sandy soil during the grouting process are presented in Figures 9 and 10.
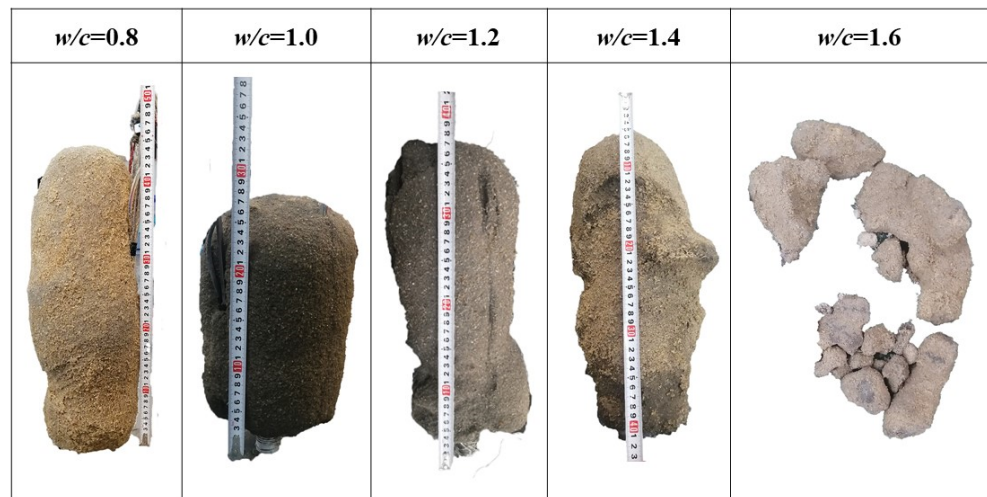

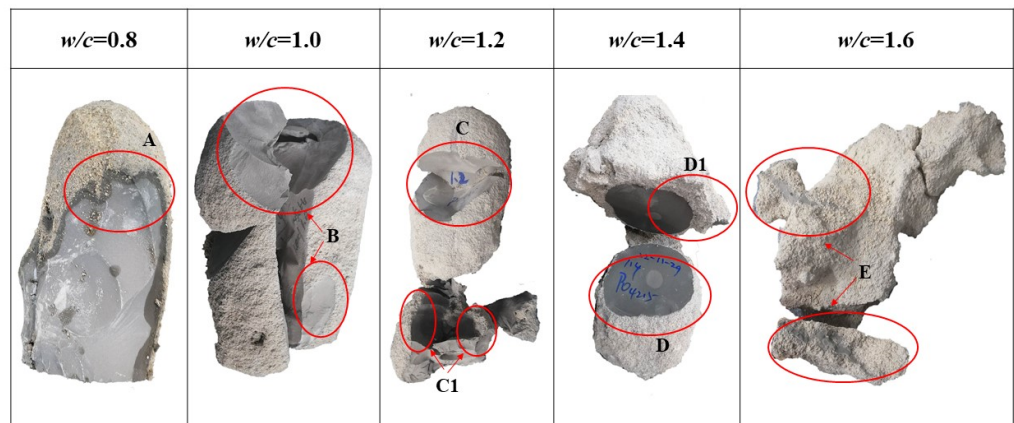**Figure 9.** Overall condition of the grout-solidified body.

Figure 10. Cross-sectional view of the grout-solidified body (The figure displays the cross-section of the solidified body, as indicated by the letters and numbers).

It can be seen from Figure 9 that the overall homogeneity of the solidified body was poorer with the increase in the *w/c* ratio. This indicated that the higher the *w/c* ratio of the grout, the more unevenly the grout was stressed within the sandy soil during the grouting process. Furthermore, when the *w/c* ratio reached 1.6, a completely solidified body cannot be formed during the grouting process.

As can be seen from the overall situation of the solidified body and the profiles at A and B presented in Figures 9 and 10, when the *w/c* ratios were 0.8 and 1.0, the solidified body was relatively uniform and mainly consisted of the pure grout, with no significant sand–grout mixture layer on the outer surface. In the case of *w/c* ratio = 1.2, a small portion of the sand–grout mixture layer with a certain thickness appeared near the grouting hole at location C1, indicating the occurrence of penetration during grouting. However, it is clear from cross-section C that the pure grout was still the primary component of the solidified body. In the case of a *w/c* ratio of 1.4, the thickness of the sand–grout mixture at location D1 increased significantly, but cross-section D still showed a predominantly pure grout solidified body. This indicated a significant penetration effect during grouting, suggesting a change in the primary interaction mode from a fracture–compaction pattern to a permeation–fracture–compaction pattern. When the *w/c* ratio increased to 1.6, the solidified body failed to form a complete solid in the soil. It is evident from cross-section E that the sand–grout mixture became the main component of the solidified body, which indicated that permeation played a major role in the grouting process. Pure grout constituted a smaller portion of the solidified body and appeared in the form of grout veins within the solidified body, with a thickness of approximately 3–5 mm. These grout veins primarily developed radially, indicating that the permeation process during grouting was accompanied by a fracturing process.

In summary, as the *w/c* ratio increased, the proportion of the sand–grout mixture in the solidified body increased. This suggested that the higher the *w/c* ratio, the less densely the grout particles were packed and the less likely they were to aggregate. When the micro-aggregates of formed grout particles were smaller than the pore size of the sandy soil, the grout could infiltrate the sandy soil. Moreover, the higher the *w/c* ratio, the smaller the grout particle micro-aggregates were, the lower the possibility of accumulation in the pore of sandy soil, the smaller the obstruction to its flow, and the more obvious the permeability. Meanwhile, as the *w/c* ratio increased, the interaction mode between the grout and the soil was transformed. The primary pattern shifted from the fracture–compaction pattern to the permeation–fracture–compaction and fracture–permeation patterns.

4.2. Analysis of Grouting Pressure Curves

A comparison of the grouting pressure curves at different *w/c* ratios is plotted in Figure 11, which shows that there were certain similarities and differences in the overall grouting pressure–time curves.

Similarity: The pressure curves for grouting followed a similar pattern of increasing to the maximum value and then decreasing. Prior to reaching the maximum, the pressure did not consistently increase with grouting time, but rather fluctuated with an overall upward trend. After reaching the maximum pressure value, the pressure maintained a downward trend.

Discrepancy: As the test process controlled the flow rate of the slurry, under different *w/c* ratios, the difference between the role of the slurry and the soil body caused the grouting pressure to show a different pattern of change over time. As shown in Figure 11, with an increase in the *w/c* ratio, the overall trend of the grouting pressure curve decreased, and the longer the grouting time required to reach the maximum value of the pressure, i.e., the slower the rate of change of the grouting pressure with time. And when *w/c* > 1.2, the overall value of the grouting pressure curve was obviously decreased, indicating that, due to the increase in the *w/c* ratio, the smaller the effect of the agglomeration of grout, the lower the formation of grout particle micro-aggregates, the smaller the blocking effect that the micro-aggregates pass through the pores of sandy soil, the smaller the resistance in the

process of slurry diffusion, which correspondingly showed the overall trend of decreasing grouting pressure, and the slower the increase in grouting pressure over time.
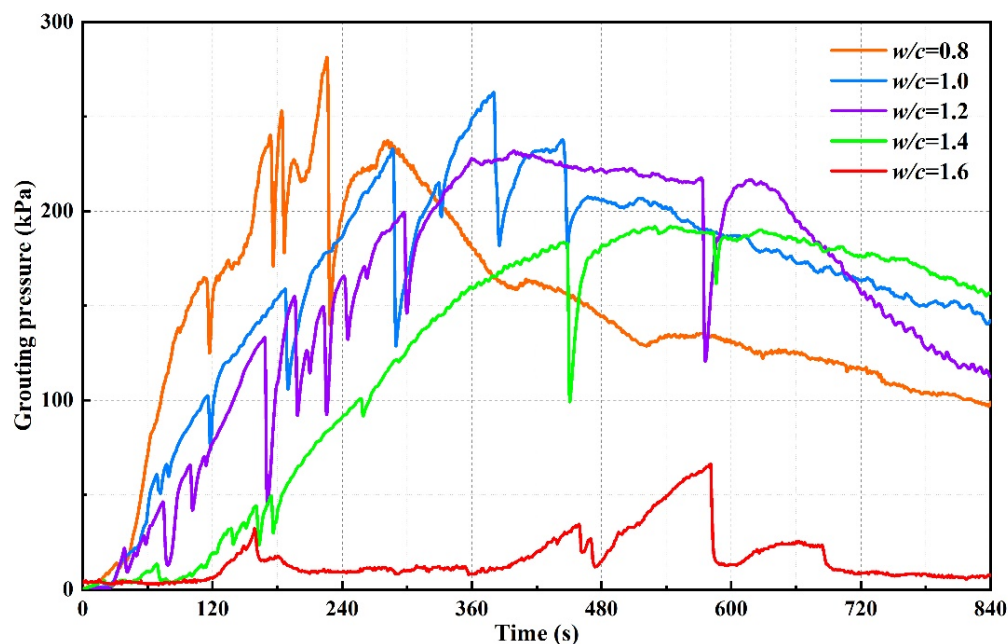

Figure 11. Variation curves of grouting pressure with time for different *w/c* ratios.

In addition, at the beginning of grouting (about 0–120 s), compared with the grouting pressure curve under the condition of *w/c* ≤ 1.2 that showed the general trend of upward change process, when *w/c* > 1.2, the pressure value was relatively stable without an obvious upward trend. Combined with the information in Section 4.1 within the grout-solidified body, it is judged that, in this low-pressure stage, when *w/c* > 1.2, the grout particle micro-aggregates could pass through the pores of the sandy soil. Therefore, the grouting pressure in this stage was relatively stable without an obvious increase. And due to the infiltration process accompanied by the filtration effect, when the pores of sandy soil were blocked by the filtration effect to form a blocking arch so that the subsequently injected grout particle micro-aggregates were blocked, the value of the grouting pressure started to show a continuous increase in the trend, as shown in the case of grouting pressure under the condition of *w/c* =1.4. Meanwhile, under *w/c* = 1.6, combined with the consolidation body situation in Section 4.1, it can be seen that infiltration in the grouting process played a major role and the size ratio of the difference between the grout particle micro-aggregates and the pore of sandy soil was large, so the filtration effect was not obvious. Thus, the grouting pressure curve and the other water–cement ratios under the conditions of the change trend were obviously different.

4.3. Variation of Surface Displacement with Time

Figures 12–15 are plotted based on the surface displacements recorded during the tests. As shown in Figures 12 and 13, in the same test, the surface displacement value exhibited a pattern of decreasing from the center of the grouting hole to the surrounding edge, i.e., the farther the horizontal distance (*D*) from the center of the grouting hole, the smaller the surface displacement value. Meanwhile, with the increase in grouting time, the uplifting speed of the surface displacement value was faster. And the farther the horizontal distance (*D*) from the center of the grouting hole, the slower the uplifting speed of the surface displacement value.
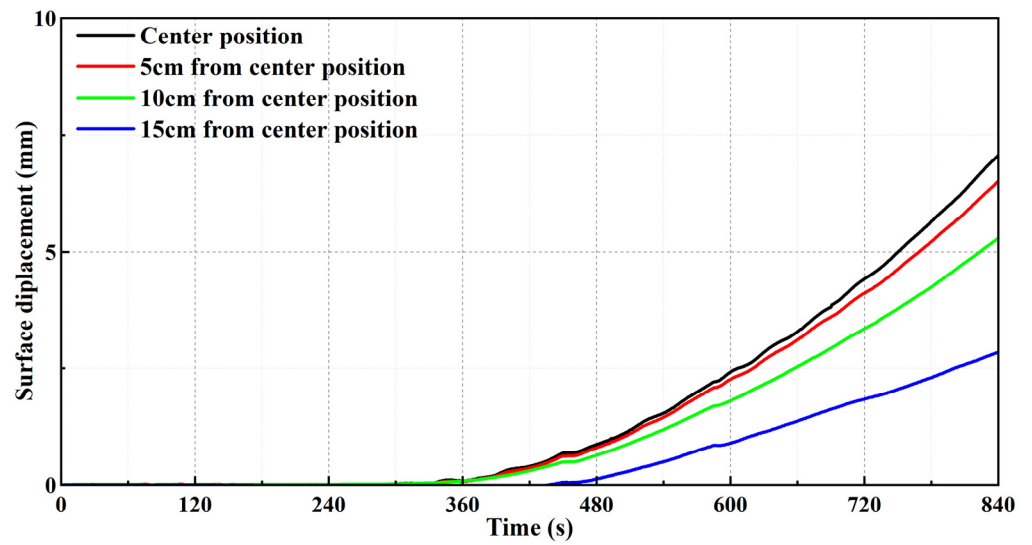
Figure 12. Variation curves of surface displacement with time for the same *w/c* ratio.
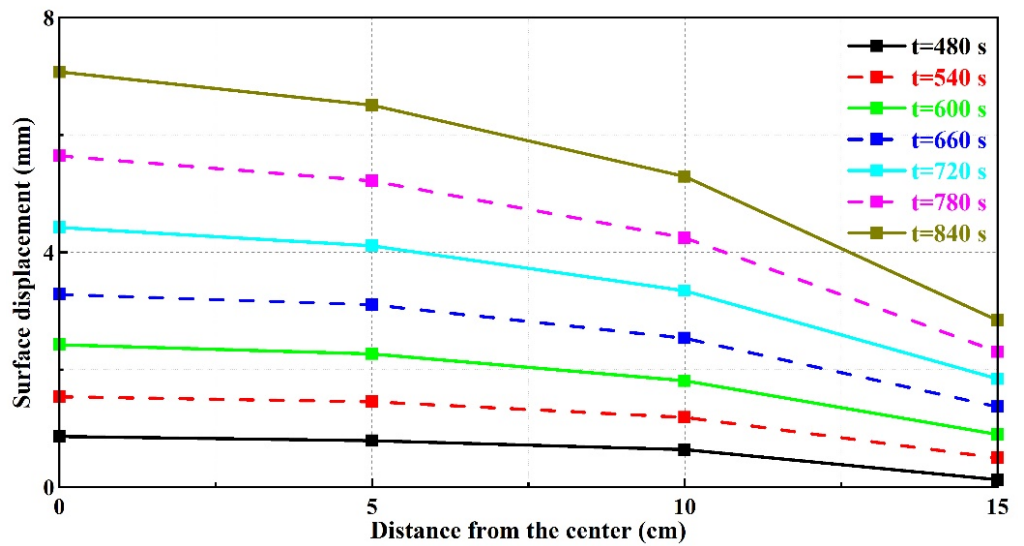

Figure 13. Variation curves of surface displacement with distance *D* from grouting center for the same water–cement ratio.
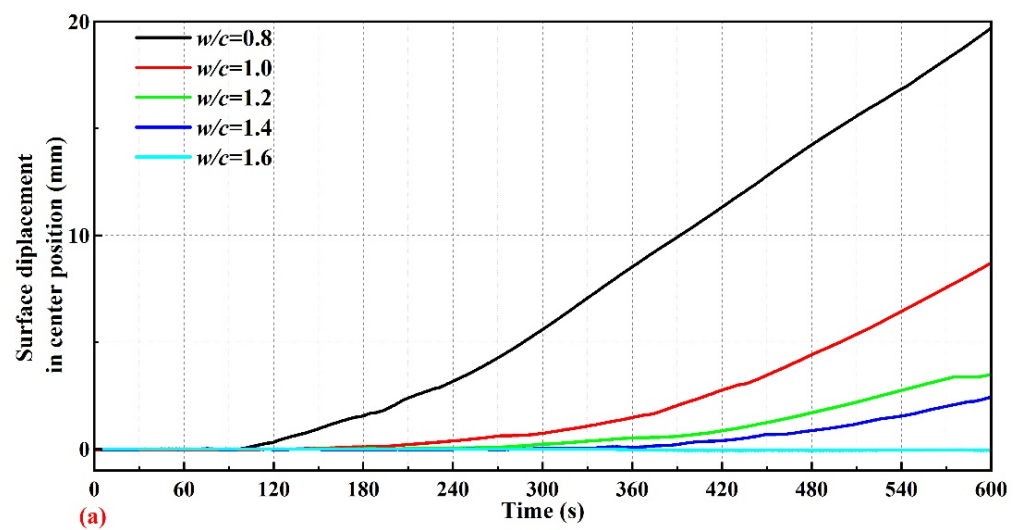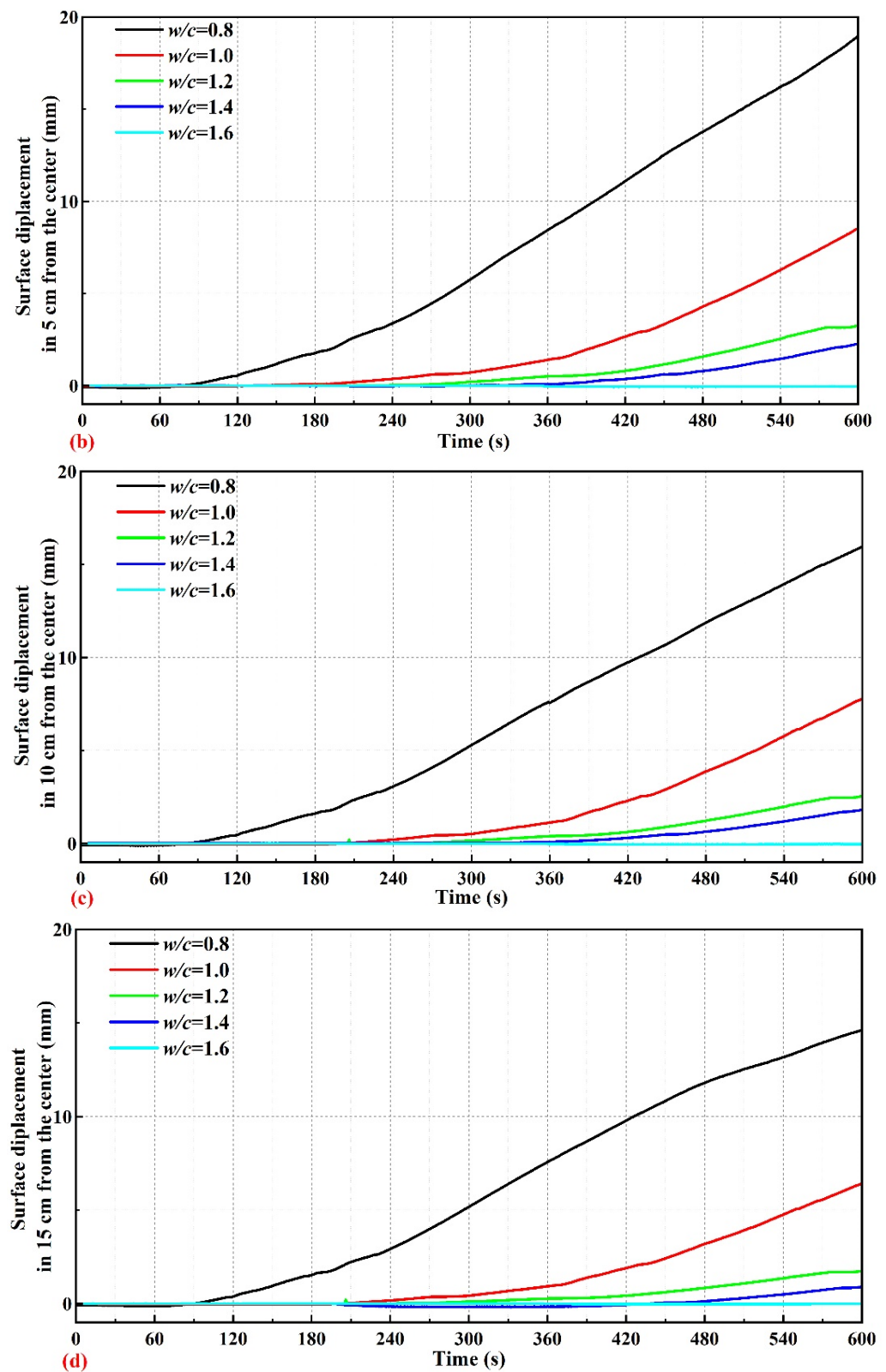

Figure 14. *Cont.*

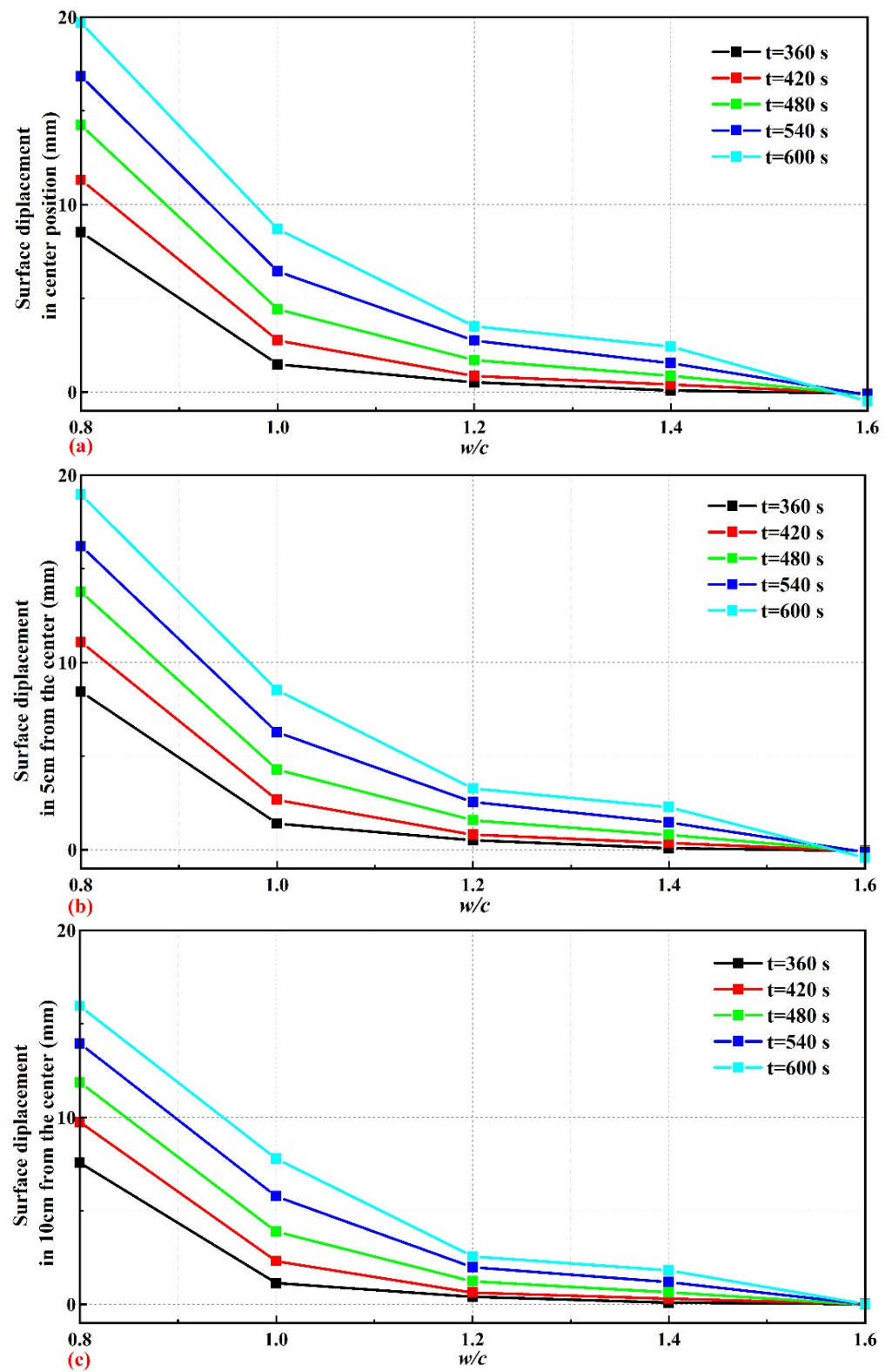**Figure 14.** Variation curves of surface displacement with time at the same locations from the center under different *w/c* ratios (**a–d**).
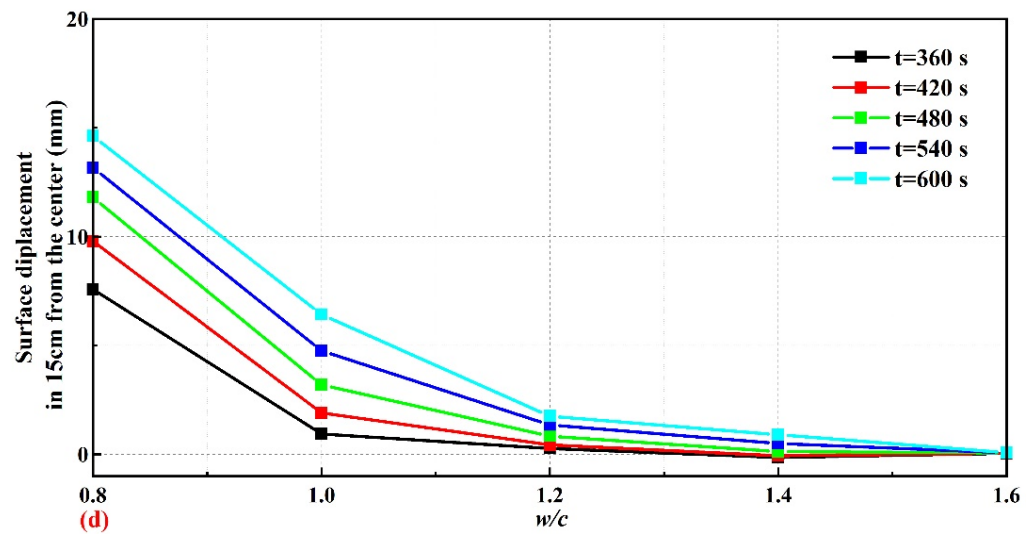
Figure 15. *Cont.*

Figure 15. Variation curves of surface displacement with *w/c* ratios at the same location (**a**–**d**).

As depicted in Figures 14 and 15, in experiments with different *w/c* ratios, an increase in the *w/c* ratio led to smaller uplift displacement values at the same location on the ground's surface within the same time period. In addition, the rate of increase in uplift values was slower, and the initiation of uplift displacement occurred later. Similarly, a longer grouting time and a larger volume of grout were required to achieve the same uplift displacement value. It can be seen from Figure 15 that the surface displacement value at the same position exhibited the maximum variation when the *w/c* ratio ranged from 0.8 to 1.0 during the same grouting time. As the *w/c* ratio exceeded 1.0, the changing trend of the surface displacement value slowed down obviously and became slower with the increasing *w/c* ratio, i.e., the decreasing change trend with the increase of *w/c* ratio slowed down with the *w/c* ratio increasing in the same grouting time. The reason for this is consistent with Section 4.1 above, and is related to the transition in the interaction mode between the grout and the sandy soil. The increase in the *w/c* ratio led to the occurrence of infiltration during grouting process in sandy soil, and the infiltration effect is more obvious in higher *w/c* ratio. Consequently, the effect of the grout on the skeleton structure in sandy soil mass decreases, leading to smaller deformations within the soil and, hence, smaller uplift displacement values at the ground's surface.

5. Conclusions

- In the grouting process with a low *w/c* ratio in the fine sand layer (under the condition of *w/c* ≤ 1.0 for the test soil), when the grouting pressure curve repeatedly reached local extrema and the corresponding surface displacement curve entered a plateau period, grout diffusion channels were formed due to soil fracture; this state was a key indicator reflecting the occurrence of the soil fracture process. The fracture–compaction grouting pattern was the main mode of the slurry diffusion process, in which the fracturing process exhibited a cyclic and non-uniform variation.

- With the advancement of grouting time, the farther away from the central grouting hole, the more pronounced the lag effect of soil pressure generated by the action of the slurry, and the larger the radius of the action of the grout on the soil. The overall soil pressures exhibited a diminishing trend with increasing distance from the grouting hole.

- As the *w/c* ratio increased, when *w/c* ≥ 1.2, the grout could penetrate the sand soil when the particle size of the grout particle micro-aggregates was less than or equal to the pore size of the sandy soil. Smaller grout particle micro-aggregates were more likely to pass through the pores of the sand, resulting in a more pronounced permeation effect. Therefore, the interaction mode between the grout and the soil

shifted from a fracture–compaction pattern to a permeation–fracture–compaction pattern and fracture–permeation pattern. The overall trend of the grouting pressure curve was similar under all of the *w/c* ratio conditions, showing the trend of increasing to the maximum value of the pressure first and then decreasing. With the increase in the water–cement ratio, the overall value of the grouting pressure curve showed a decreasing trend, the slower the pressure value increased with time before reaching the maximum value, and the more obvious the influence of water–cement ratio was when *w/c* > 1.2. In addition, as the *w/c* ratio increased, the resistance encountered by the grout particle micro-aggregates passing through the pores of the sandy soil decreased and the sand body became smaller due to the slurry deformation effect, leading to a reduction in the effect of the grout on the sandy soil mass. As a result, the surface displacement also exhibited an overall decreasing trend, and it had no obvious lifting value under the condition of *w/c* = 1.6.

Author Contributions: Conceptualization, H.H. and C.D.; methodology and test, H.H., Y.L., C.D., B.G., Z.X., Y.C. and A.C.; formal analysis, Y.L.; data curation, Y.L., B.G. and Z.X.; writing—original draft preparation, Y.L.; writing—review and editing, H.H., Y.L. and C.D.; project administration, H.H. and C.D.; funding acquisition, H.H. and C.D. All authors have read and agreed to the published version of the manuscript.

Data Availability Statement: The data used in this study are available from the corresponding author on reasonable request.

Conflicts of Interest: The authors declare no conflicts of interest.

Abbreviations

w/c ratios	water-to-cement ratios,
H	vertical height from the bottom of the bucket,
D	radial distance from the center of the grouting hole

References

1. Liu, H.; Shi, Z.; Li, Z.; Wang, Y. Experimental Investigation on Reinforcement Application of Newly Permeable Polymers in Dam Engineering with Fine Sand Layers. *Water* **2023**, *15*, 3761. [CrossRef]
2. Park, D.; Oh, J. Permeation grouting for remediation of dam cores. *Eng. Geol.* **2018**, *233*, 63–75. [CrossRef]
3. Rasouli, R.; Hayashi, K.; Zen, K. Controlled Permeation Grouting Method for Mitigation of Liquefaction. *J. Geotech. Geoenvironmental Eng.* **2016**, *142*, 04016052. [CrossRef]
4. Yuan, S.; Zhang, G.; Zheng, G.; Cai, F.; Qian, Z. Grouting treatment of water and sand inrush into an included shaft in aeolian sand layer. *J. China Coal Soc.* **2018**, *43*, 1104–1110. [CrossRef]
5. Xu, S.; Cao, H.; Zhu, Y.; Sun, H.; Lu, J.; Shi, J. Mechanism of Filtration Behaviors of Cement-Based Grout in Saturated Sand under Different Grouting Conditions. *Geofluids* **2022**, *2022*, 2332743. [CrossRef]
6. Zhang, L. Study on Penetration and Reinforcement Mechanism of Grouting in Sand Layer Disclosed by Subway Tunnel and Its Application. Ph.D. Thesis, Shandong University, Jinan, China, 2017.
7. Elwakil, A.Z.; Azzam, W.R. Soil improvement using grout walls. *Alex. Eng. J.* **2016**, *55*, 2741–2748. [CrossRef]
8. Guo, C.; Hu, D.; Wang, F. Diffusion Behavior of Polymer Grouting Materials in Sand and Gravel. *Soil Mech. Found. Eng.* **2021**, *57*, 440–444. [CrossRef]
9. Fraccica, A.; Spagnoli, G.; Romero, E.; Arroyo, M.; Gómez, R. Permeation grouting of silt-sand mixtures. *Transp. Geotech.* **2022**, *35*, 100800. [CrossRef]
10. Sha, F.; Li, S.; Lin, C.; Liu, R.; Zhang, Q.; Yang, L.; Li, Z. Research on penetration grouting diffusion experiment and reinforcement mechanism for sandy soil porous media. *Rock Soil Mech.* **2019**, *41*, 4259–4269. [CrossRef]

11. Yoon, J.; El Mohtar, C.S. A filtration model for evaluating maximum penetration distance of bentonite grout through granular soils. *Comput. Geotech.* **2015**, *65*, 291–301. [CrossRef]
12. Zhou, F.; Xu, Y.; Zhu, R.; Song, Z.; Zhai, D.; Mou, Y. Diffusion Characteristics of Grouting Slurry in Sandy Stratum. *J. Archit. Civ. Eng.* **2020**, *37*, 182–192. [CrossRef]
13. Feng, X.; Liu, R.; Li, S.; Han, W.; Zhao, S.; Wang, H. Characteristics of moving interface of grout considering deep bed filtration. *Chin. J. Rock Mech. Eng.* **2016**, *35*, 1000–1008. [CrossRef]
14. Li, S.; Feng, X.; Liu, R.; Zhang, L.; Han, W.; Zheng, Z. Diffusion of grouting cement in sandy soil considering filtration effect. *Rock Soil Mech.* **2017**, *38*, 925–933. [CrossRef]
15. Yang, Z.; Hou, K.; Cheng, Y.; Yang, B. Study of column-hemispherical penetration grouting mechanism based on power-law fluid. *Chin. J. Rock Mech. Eng.* **2014**, *33*, 3840–3846. [CrossRef]
16. Yang, Z.; Hou, K.; Liang, W.; Cheng, Y.; Yang, B. Study of diffusion parameters of Newtonian fluid based on column-hemispherical penetration grouting. *Rock Soil Mech.* **2014**, *35*, 17–24. [CrossRef]
17. Zhang, Q.; Wang, H.; Liu, R.; Li, S.; Zhang, L.; Zhu, G.; Zhang, L. Infiltration grouting mechanism of porous media considering diffusion paths of grout. *Chin. J. Geotech. Eng.* **2018**, *40*, 918–924. [CrossRef]
18. Bao, X.; Zhang, Y.; Xu, C.; Fu, Y.; Cui, H.; Xie, X. Factors Affecting the Settlement of Double-Line Shield Tunnel Construction. *J. Chongqing Jiaotong Univ. (Nat. Sci.)* **2020**, *39*, 51–60. [CrossRef]
19. Fu, Y.; Chen, X.; Wu, P. Analysis on Mechanism of Longitudinal Grouting Uplift of Existing Metro Tunnel. *Mod. Tunn. Technol.* **2020**, *57*, 184–192. [CrossRef]
20. Hamderi, M.; Gallagher, P.M. Pilot-scale modeling of colloidal silica delivery to liquefiable sands. *Soils Found.* **2015**, *55*, 143–153. [CrossRef]
21. Ye, X.; Wang, S.; Zhang, S.; Xiao, X.; Xu, F. The compaction effect on the performance of a compaction-grouted soil nail in sand. *Acta Geotech.* **2020**, *15*, 2983–2995. [CrossRef]
22. Yi, X.; Zhang, D.; Pang, T.; Luo, J. Practice and monitoring analysis of building lifting due to grouting. *Rock Soil Mech.* **2009**, *30*, 3776–3782. [CrossRef]
23. Zhang, Z.; Zou, J.; He, J.; Wang, H. Chinese Journal of Geotechnical Engineering. *Lab. Tests Compact. Grouting Fract. Grouting Clay* **2009**, *31*, 1818–1824.
24. Wang, Q.; Wang, S.; Sloan, S.W.; Sheng, D.; Pakzad, R. Experimental investigation of pressure grouting in sand. *Soils Found.* **2016**, *56*, 161–173. [CrossRef]
25. Ye, X.; Wang, S.; Wang, Q.; Sloan, S.W.; Sheng, D. The influence of the degree of saturation on compaction-grouted soil nails in sand. *Acta Geotech.* **2019**, *14*, 1101–1111. [CrossRef]
26. Li, P.; Zhang, Q.; Zhang, X.; Li, S.; Zhang, W.; Li, M.; Wang, Q. Analysis of fracture grouting mechanism based on model test. *Rock Soil Mech.* **2014**, *35*, 3221–3230. [CrossRef]
27. Li, S.; Zhang, W.; Zhang, Q.; Zhang, X.; Liu, R.; Pan, G.; Li, Z.; Che, Z. Research on advantage-fracture grouting mechanism and controlled grouting method in water-rich fault zone. *Rock Soil Mech.* **2014**, *35*, 744–752. [CrossRef]
28. Zhang, L.; Li, Z.; Liu, R.; Zhang, Q.; Li, S. Simulation tests on fracture-compaction grouting process in sand layer. *Chin. J. Geotech. Eng.* **2019**, *41*, 665–674. [CrossRef]
29. Zhang, L.; Li, Z.; Zhang, Q.; Liu, R.; Li, S. Compaction behavior of sand layer and its effect on diffusion process of fracture-compaction grouting mode. *J. China Coal Soc.* **2020**, *45*, 667–675. [CrossRef]
30. Zhang, L.; Li, Z.; Zhang, Q.; Liu, R.; Zhang, X.; Yu, W. Split grouting mechanism based on nonlinear characteristics of compression process of soil. *Chin. J. Rock Mech. Eng.* **2016**, *35*, 1483–1493. [CrossRef]
31. Qin, P.; Sun, H.; Chen, X.; Yang, G.; Liang, Y. Analysis of splitting grouting mechanism considering sand compaction characteristics. *Exp. Technol. Manag.* **2023**, *40*, 31–37+43. [CrossRef]